International Journal of Precision Engineering and Manufacturing (2022) 23:929–942
https://doi.org/10.1007/s12541-022-00661-y

Online ISSN 2005-4602
Print ISSN 2234-7593

REGULAR PAPER

Design of High-Durability Superhydrophobic Microsurface Structures

Yousung Kang[1] · Gayun Jang[1] · Ga Eul Kim[2] · Sin Kwon[2] · Moon G. Lee[1] · Yongho Jeon[1]

Received: 11 November 2021 / Revised: 28 February 2022 / Accepted: 18 April 2022 / Published online: 15 June 2022

Abstract
The development of industrial technology has increased the demand for surface modification to functionalize product surfaces. Superhydrophobicity affords a self-cleaning ability and is highly regarded in various industrial fields. However, superhydrophobic surfaces are limited in terms of their mechanical and chemical durability, which must be addressed to allow them to advance to the commercialization stage. In this study, we proposed a hierarchical structure to increase the durability of a microsurface exhibiting superhydrophobicity. It was optimized based on a design of experiments and finite element analysis. Results of the finite element analysis indicated that the maximum stress of the proposed hierarchical structure reduced by approximately 71% compared to that of the well-known pillar structure. The wettability and durability of the superhydrophobic film fabricated via micro three-dimensional printing and ultraviolet-imprint lithography were evaluated. The optimal hierarchical structure yielded a contact angle of 150° or more, and the change in the contact angle change was within 5° even after 10,000 cycles of the abrasion test.

Keywords Superhydrophobic · Mechanical durability · Design of experiments · Projection microstereolithography · Pin on disc abrasion test

1 Introduction

As the technology level of modern industry advances, interest in the high functionality and surface modification of product surfaces is increasing. Additionally, studies pertaining to changing the properties of the material surface by simulating surface properties observed in nature are increasing. Among them, studies regarding superhydrophobic surfaces inspired by the surface structure of lotus petals are actively being conducted.

A superhydrophobic surface refers to a surface that forms a contact angle of 150° or more with water. These surfaces afford self-cleaning ability [1, 2] and drag reduction [3, 4], as well as prevent contamination, freezing [5], and corrosion [6]. Hence, they exhibit potential application in various industries such as, architecture, display, optics, medical [7, 8], aviation, and transportation [9–13].

The surface of the lotus leaf is composed of a nano/microscale protrusion structure and a coating layer with low surface energy [14, 15]. A surface structure with low surface energy and high surface roughness is required to exhibit high repulsive properties with respect to water [16].

The surface processing of nano/microstructures involves bottom-up and top-down methods. Bottom-up processes include self-assembly [17], chemical deposition [18], electroplating [19, 20], and plasma treatment [21]. This method involves coating the surface of a base material with a nanoparticle or molecular structure and is characterized by the random generation of a surface structure. The top-down method includes photolithography [22], lasers [23, 24], plasma, and etching [25], and may be used to process a regular surface structure. A general superhydrophobic surface comprises micropillar arrays; recently, research has been conducted on a hierarchical structure in which a nano/microscale structure is formed on a microsurface structure via a hybrid method involving the bottom-up and top-down methods. This method is expected to increase the surface roughness and contact angle by changing the surface energy.

✉ Yongho Jeon
princaps@ajou.ac.kr

[1] Department of Mechanical Engineering, Ajou University, 206, World cup-ro, Yeongtong-gu, Suwon-si 16499, Gyeonggi, Korea

[2] Department of Printed Electronics, Nano-Convergence Manufacturing Systems Research Division, Korea Institute Machinery Materials (KIMM), Daejeon-si 34103, Korea

The hybrid method is being investigated by combining various processes. Sun et al. proposed a method for processing pillar arrays on silicon wafers via photolithography and plasma etching, as well as depositing carbon nanotubes on a surface via chemical vapor deposition [26]. Wang et al. proposed a method for processing a microcone structure on a copper substrate using a picosecond laser, as well as processing a nanoscale surface structure through electroplating [27]. N. Kehagias et al. coated Cr and Au layers via electron beam deposition and then processed a pillar array via Ni electroplating [28]. Alameda et al. proposed a method for processing a layered structure by combining nanoimprint and photolithography processes [22]. Shivaprakash et al. proposed a surface processing method that involves roll-to-roll hot embossing [29]. Lin et al. proposed a method involving two-photon polymerization [30]. Dong et al. proposed a method involving direct laser writing [31].

As such, various processes have been proposed for surface processing using a nano/microscale hierarchical structure. However, photolithography-based three-dimensional (3D) microsurface processing requires a separate photomask for each layer and involves complicated subsequent processes. In addition, to commercialize the superhydrophobic surface, the mechanical durability of the coating layer or nano/microstructure due to surface modification must be ensured. If the mechanical durability of the surface is low, then the surface will deteriorate easily; consequently, its surface characteristics are diminished, and defects are generated [32, 33].

X. Chen et al. coated the surface on a stainless steel surface via TiO_2 plasma spraying and evaluated the abrasion resistance using #800 sandpaper under a 25 kPa load [34]. Liu et al. formed a surface structure via electroplating and performed an evaluation using #1000 sandpaper under a 1.3 kPa load [19]. Xiu et al. compared the durability of a surface based on the material by forming a coating layer on the surface of a polyurethane film and Si metal via Ar and SF6 plasma treatment, and 0.25 m abrasion under a 225 g load using a polyester wiper fabric [35]. In a study by Xiu, the contact angle before and after wear on the surface of the polyurethane film decreased from 168° to 138.7°, and the contact angle hysteresis increased from $\leq 2°$, to $\geq 60°$. By contrast, it was reported that the contact angle of Si metal surface did not change significantly, i.e., from 168.1° to 167.4°, and the contact angle hysteresis was increased from $\leq 2°$ to $13.6 \pm 3°$. Hence, it can be confirmed that the structure of a polymer-based surface is more vulnerable to mechanical wear than the surface of metal. In addition, Golovin et al. formed a surface structure via the mixing reaction of a coating solution based on spray coating and evaluated its durability by performing a wear test. It was reported that the spray-coated surface was maintained through self-healing by mixing fluorinated polyurethane elastomer and 1H, 1H, 2H, 2H-heptadecafluorodecyl polyhedral oligomeric silsesquioxane [33].

As such, research pertaining to the durability of superhydrophobic surfaces has primarily been conducted to investigate the bonding force and wear resistance of a coating layer formed bottom-up on a metal surface. Furthermore, a method to continuously expose a material surface with low surface energy even after wear healing was identified. In particular, according to Xiu et al., a surface structure formed using polymer materials is weaker in terms of durability than one formed using metals. Nonetheless, investigations into shape designs that can ensure the durability of super water repellent surfaces using the top-down method are insufficient. In this study, a robust structure that maintains the surface structure even when the superhydrophobic surface of a polymer material is exposed to a mechanical wear environment was designed. The stress analysis of a general micropillar structure was performed using the finite element method, and the optimal design for reducing the maximum stress generated in the surface structure was identified under the same load conditions used in the design of experiments. Thereafter, a prototype with an optimal design shape was processed using micro 3D printing, and a microsurface structure was formed on a polyethylene terephthalate (PET) film using a polydimethylsiloxane (PDMS) mold and an ultraviolet (UV)-imprint lithography process. A pin-on-disc experiment was conducted using a silicone rubber tip to evaluate the durability of the processed surface.

2 Design of Surface Structure

2.1 Numerical Analysis of Micropillar

Wenzel [36] and Cassie–Baxter [37] models are typical models used to explain the wetting characteristics of a surface. Based on the Cassie–Baxter model, a smaller solid contact area compared with the liquid contact area results in a higher contact angle. This implies that the surface's contact angle increases with the surface roughness. In general, a superhydrophobic surface increases the roughness of a surface through a pillar-shaped structure, which is vulnerable to shear loads.

A finite element analysis was performed to analyze the stress distribution generated on a pillar-shaped structure subjected to a load. The reference model was a cylindrical micropillar structure, and it was assumed that a residual film with a thickness of 10 μm was present. A fillet structure with a radius of 0.5 μm was added and modeled considering the stress concentration of the micropillar structure under load conditions. The mesh shape and dimensions of the reference model are presented in Fig. 1 and Table 1, respectively. ANSYS Workbench 2019R3 was used as the

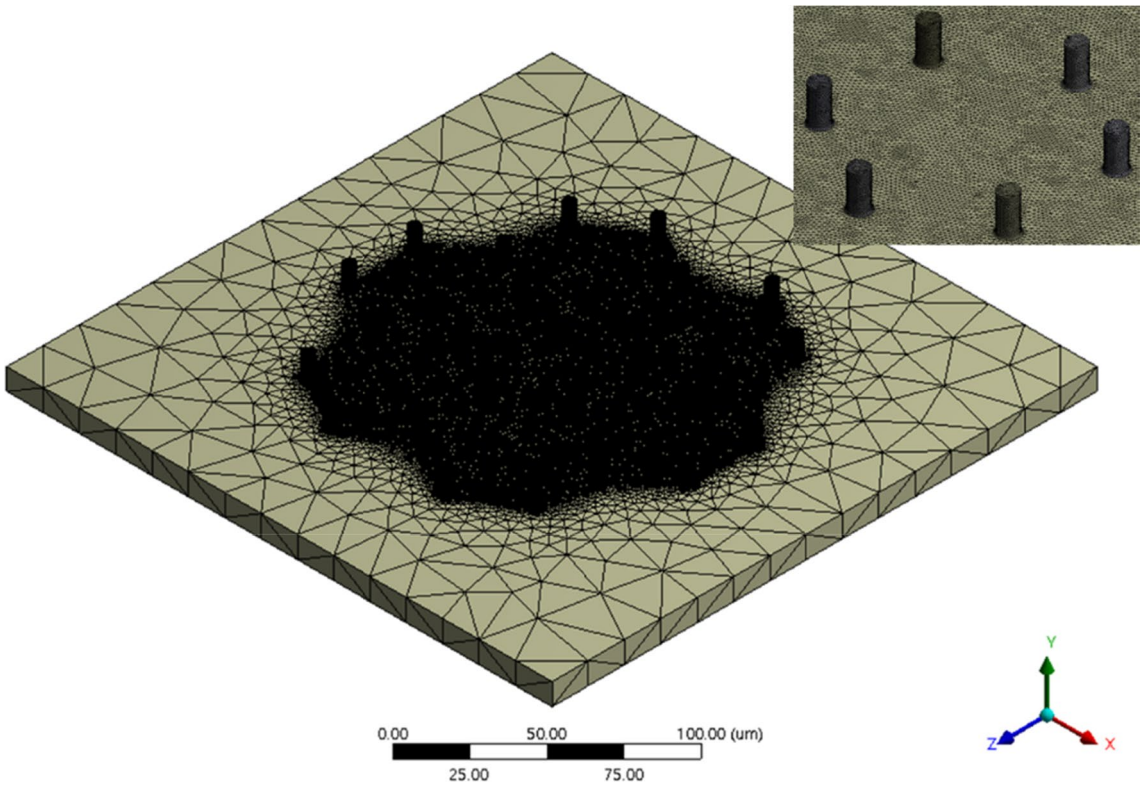

Fig. 1 Modeling for structural analysis of micropillar structures. Numbers of elements and nodes are 479,784 and 730,658, respectively

Table 1 Geometric parameters of micropillar structure

Parameter	Value (μm)
Diameter of pillars	5
Height of pillars	10

finite element analysis software, and the mesh size of the analysis model was set to 0.5 μm. The elastic modulus of the analysis model was 2.7 GPa, the density was 950 kg/m^3, and the Poisson ratio was 0.34. For the boundary conditions, the bottom surface of the residual film was set to a fixed support. For the load conditions, a shear load of 0.5 MPa was applied to the X- and Z-axes, and a compressive load of 0.5 MPa was applied to the Y-axis which corresponds to the compression direction. We assume a situation that applies mechanical pressure to the hydrophobic surface with a person's finger. Assuming that the finger's contact area is 350–420 mm^2 depending on gender [38], it corresponds to a load of approximately 175–230 N. In addition, by applying the corresponding pressure to each axis, analysis and optimal design is carried out in consideration of more severe conditions than the general situation. Figure 2 shows the stress distribution when a load of 0.5 MPa was applied to each axis of the micropillar structure. It was confirmed that a maximum stress of 16.83 MPa was generated, and that the stress was concentrated at the lower end of the pillar.

2.2 Design for High Durability Pillar Structure

The stress distribution generated under conditions in which compression and shear loads impacted the micropillar structure were analyzed. When a load is exerted on the micropillar structure, a defect may occur, as the stress is concentrated at a point crossing the residual film. To disperse the stress concentration of the micropillar structure, a partition wall structure lower than the pillar height was added between each pillar to achieve a hierarchical structure. The finite element analysis model of the hierarchical structure is shown in Fig. 3, and the shape information is presented in Table 2. The physical properties, grid size, and boundary conditions were applied in the same manner as the analysis models shown in Figs. 1 and 2.

Compared with the maximum stress generated, as shown in Fig. 2, the maximum stress of 7.93 MPa decreased by approximately 52.8% in the layered structure, to which the partition wall structure was added. Hence, it was confirmed that the partition wall structure effectively relieved the stress concentration generated in the micropillar structure. To maximize the effect of relieving the stress concentration using the partition wall structure, an optimal design was determined based on the experimental design (Fig. 3).

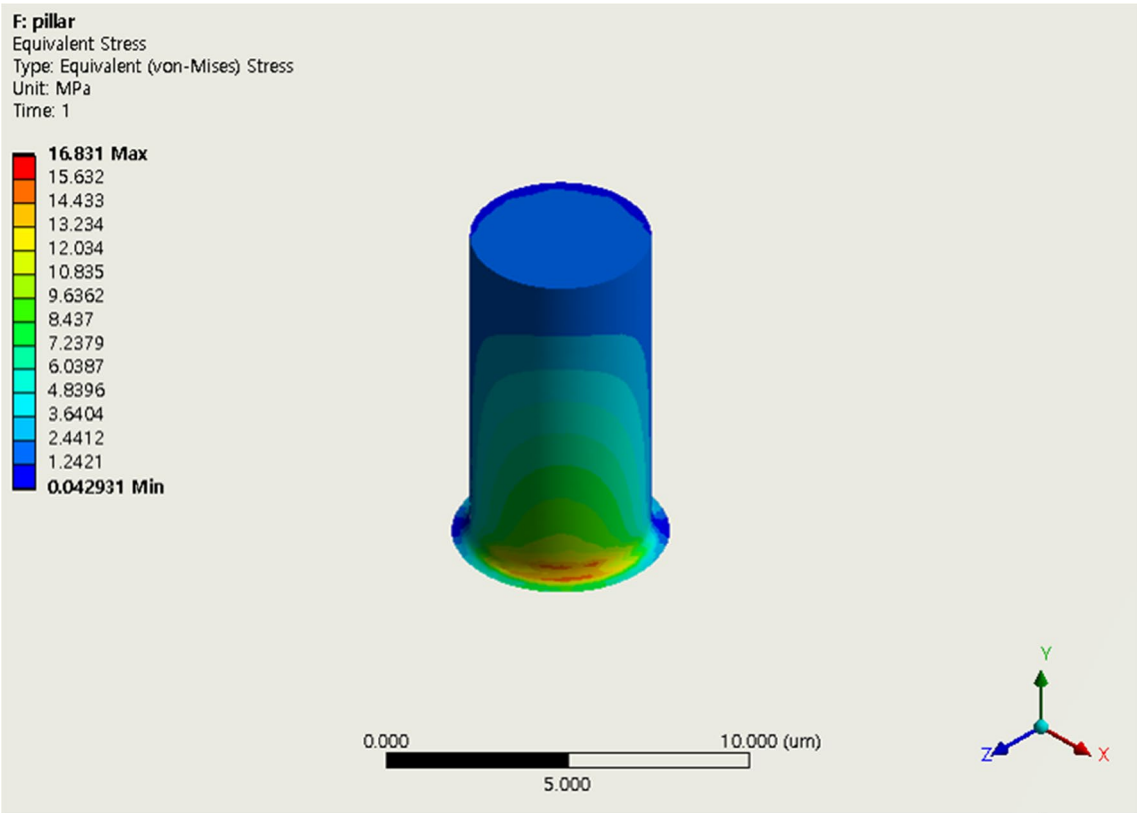

Fig. 2 Stress concentration of micropillar structure. Stress concentration occurred at intersection of residual layer

2.3 Design Optimization for Hierarchical Pillar Structure

To maximize the stress concentration relief effect of the micropillar structure using the wall structure, an optimal design was determined based on the design of experiments. Design factors were selected as shown in Table 2; the level gap was set to level 3, the distance between the pillars was set to 10 μm, and the level gap of the remaining factors was set to 1 μm. After each simulation case was modeled, a finite element analysis was performed under the same physical properties, grid size, boundary conditions, and load conditions, as shown in Figs. 1 and 2. Table 3 shows the orthogonal arrangement table used for the optimal design and analysis results for each experimental condition. A sensitivity analysis was conducted to confirm the change in the maximum stress based on the change in the level of each design factor shown by the results in Table 3.

The results of the sensitivity analysis are shown in Fig. 4. Within the level range of each factor, when the diameter of the lower end was larger than the diameter of the upper end of the pillar, a lower maximum stress was generated. In addition, although it was lower than the pillar height, the larger the height of the partition wall between them, the lower was the maximum stress generated. It was observed that the load dispersed as the cross-sectional area increased toward the bottom of the structure. Meanwhile, it was confirmed that the change in the thickness of the partition wall and the distance between the pillars indicated less change in terms of the maximum stress distribution compared with the change in the level of other design factors.

Based on the results of the sensitivity analysis, the shape in which the maximum stress was generated when the minimum load was applied was selected. The design variables of the selected shape were as follows: upper diameter, 4 μm; lower diameter, 6 μm; pillar height, 9 μm; partition wall height, 6 μm; partition wall thickness, 6 μm; pillar-to-pillar distance, 20 μm.

The optimal shape was modeled, and the maximum stress was confirmed by applying the same physical properties, mesh size, boundary conditions, and load conditions. The results of the finite-element analysis of the optimal shape are shown in Fig. 5. Compared with the micropillar structure shown in Fig. 2, a maximum stress of 4.88 MPa was generated, which was a reduction by approximately 71%.

Because the design factors selected in Table 2 can be applied regardless of the shape of the partition wall, triangular and rectangular partition wall structures were applied and compared in addition to the hexagonal partition wall shown in Fig. 5. Table 4 presents the results of the changes in the

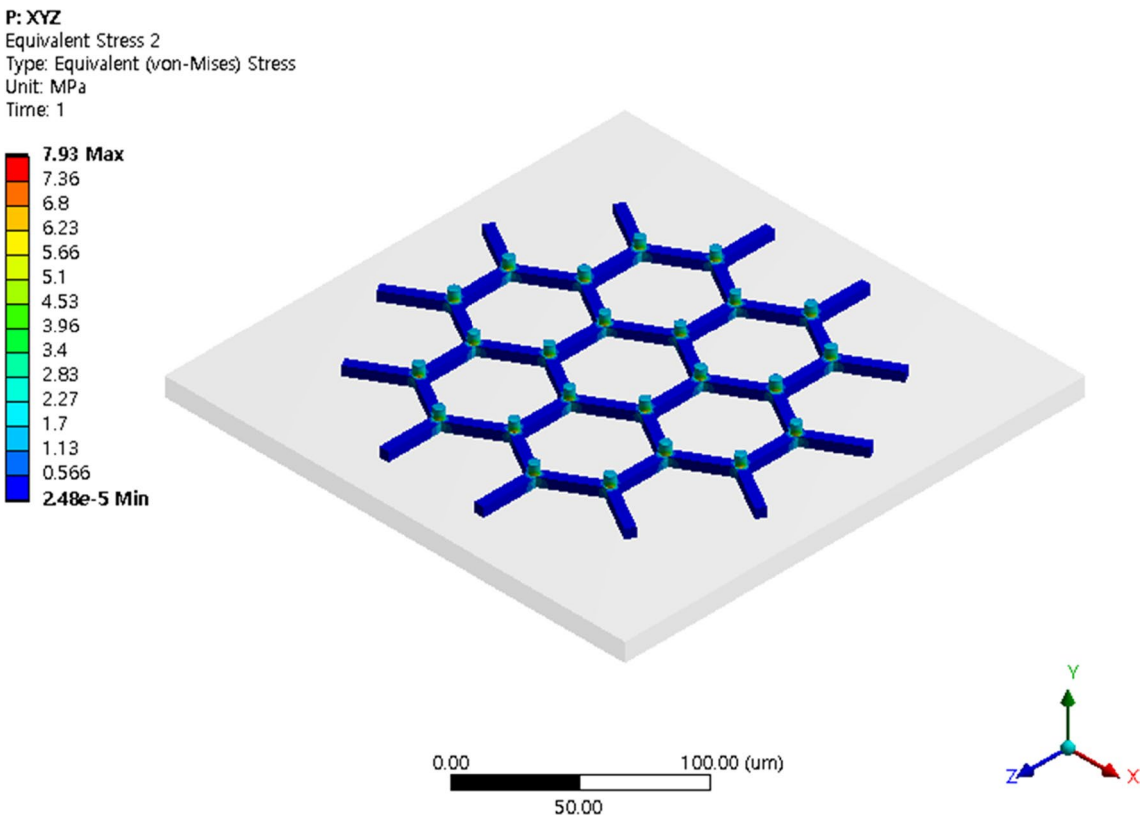

Fig. 3 Stress distribution results of proposed micropillar hierarchical structure to reduce stress concentration. Numbers of elements and nodes are 2,569,925 and 3,670,820, respectively

Table 2 Geometric parameters of hierarchical structure

Parameter	Value (μm)
Top diameter of pillars	5
Bottom diameter of pillars	5
Height of pillars	10
Thickness of bulkheads	5
Height of bulkheads	5
Spacing between pillars	30

partition wall structure. Regardless of the change in the partition wall structure, it was confirmed that the distribution of the maximum stress generated was narrower compared with that of the surface composed of only micropillars.

3 Fabrication of Microsurface

3.1 Prototyping via Micro 3D Printing

A prototype of the surface where the optimal design was applied was processed via projection microstereology (PμSL). The PμSL process is a method of stacking and manufacturing micropatterns using a digital micromirror device as a virtual photomask. A BMF MicroArch S130 equipment was used for the prototype processing. The optical resolution of the MicroArch S130 equipment was 2 μm, and the thickness of the stacked layer was 5–20 μm. Because the thickness of the stacked layer of the equipment was limited by the thickness of the optimal shape, the prototype was expanded by five times. The material used in the PμSL process is a photo-curable resin (HTL yellow trans resin, BMF Inc.). The cured resin has a tensile strength of 57 MPa, a modulus of elasticity of 3 GPa, and a hardness of 81 shore D. An optical microscope image of the processed surface is shown in Fig. 6.

3.2 Fabrication via UV-Imprint Lithography

The surface processed via PμSL was replicated on a PET film via UV-imprint lithography. First, a reverse-phase mold was manufactured using PDMS. Thereafter, PDMS was placed in contact with the PET film, to which photocurable PUA resin was applied and then exposed to UV to obtain the same surface structure as the prototype. Figure 7 shows a schematic illustration of the reproduction pattern processing using UV-imprint lithography. The photocurable PUA

Table 3 Results of finite element analysis from orthogonal arrangement table

Case	Design factor						Maximum stress (MPa)
	A	B	C	D	E	F	
1	1	1	1	1	1	1	12.79
2	1	1	1	1	2	2	10.77
3	1	1	1	1	3	3	8.65
4	1	2	2	2	1	1	10.47
5	1	2	2	2	2	2	9.41
6	1	2	2	2	3	3	8.21
7	1	3	3	3	1	1	8.51
8	1	3	3	3	2	2	8.16
9	1	3	3	3	3	3	7.64
10	2	1	2	1	1	2	16.72
11	2	1	2	1	2	3	14.4
12	2	1	2	1	3	1	11.05
13	2	2	3	2	1	2	16.43
14	2	2	3	2	2	3	14.37
15	2	2	3	2	3	1	13.04
16	2	3	1	3	1	2	9.43
17	2	3	1	3	2	3	8.5
18	2	3	1	3	3	1	7.21
19	3	1	3	1	1	3	24.09
20	3	1	3	1	2	1	19.87
21	3	1	3	1	3	2	15.68
22	3	2	1	2	1	3	12.98
23	3	2	1	2	2	1	10.34
24	3	2	1	2	3	2	8.43
25	3	3	2	3	1	3	14.36
26	3	3	2	3	2	1	12.7
27	3	3	2	3	3	2	11.07

A top diameter of pillar (4, 5, and 6 μm), *B* bottom diameter of pillar (4, 5, 6 and μm), *C* pillar height (9, 10, and 11 μm), *D* thickness of partition wall (4, 5, and 6 μm), *E* height of partition wall (4, 5, and 6 μm); and *F* interval between pillars (20, 30, and 40 μm)

resin used was MINS-311RM (Minuta Technology), and the UV curing machine used was MT-UV-A48 (Minute Technology). Figure 8 shows the scanning electron microscopy (SEM) image of the reference shape and the optimal shape pattern replicated on the PET film.

4 Performance Tests Using Imprinted Film

4.1 Wettability Test

Contact angle measurements of the imprint film processed via PμSL and UV-imprint lithography were performed using an OCA 15EC equipment (Data Logistics), and the measurements were performed for more than three times by moving the measurement position. The droplet volume was measured to be 5 μL using a Pipetman Classic P10 micropipette (Gilson). CF_4 plasma treatment was performed using an SNTEK ERR-5006 RIE SYSTEM equipment to reduce the surface energy of the imprint film. The plasma treatment conditions were as follows: RF power, 40 W; gas flow rate, 40 sccm; processing time, 3 min; pressure, 250 mTorr.

Figure 9 shows the contact angle values due to the change in the partition wall structure and plasma treatment. The reference structure in Fig. 9 means the hexagonal partition wall structure without optimization. The contact angle of the surface with CF_4 plasma treatment under the same conditions is 158.7° in the reference structure, and the optimal structure is 154.1°. Even in the optimal structure, a more than 150° contact angle is realized. The difference in contact angle between the reference structure and the optimal structure is affected by the fraction of the solid contact area. The distance between the reference structure and the pillar of the optimal structure is 30 μm and 20 μm, respectively, so there is a difference in the solid contact area fraction. The larger the fraction of the solid contact area to the liquid contact

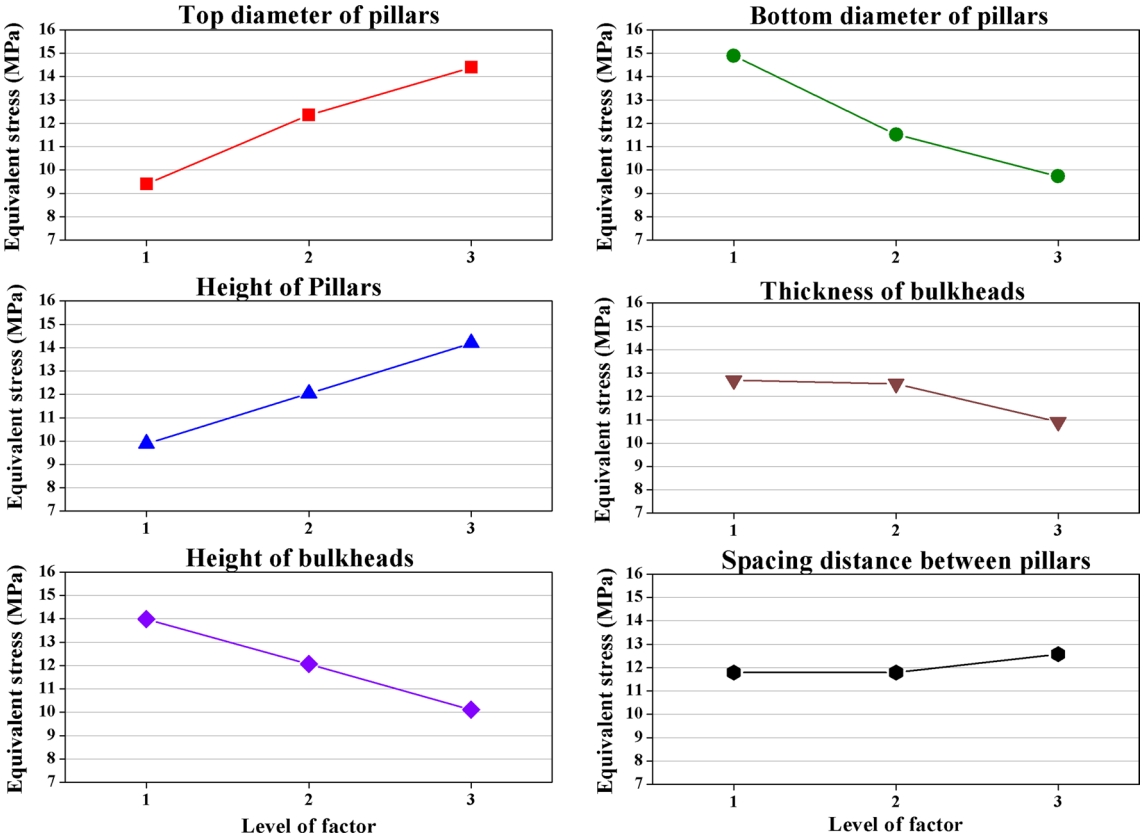

Fig. 4 Results of sensitivity analysis for amount of change in maximum stress based on level change of each factor

area by the Cassie–Baxter model, the lower was the contact angle. Because the contact angle was measured by fixing the size of the water droplets, it can be assumed that the area in contact with the liquid remained the same. The fraction of the solid contact area decreased in the following order: triangular, rectangular, and hexagonal partition wall structures. In the triangular partition wall structure with a high solid contact area fraction, the contact angle was relatively low, whereas the contact angle was relatively high in the hexagonal partition wall structure with a low solid contact area fraction. In addition, as the surface energy decreased via the CF_4 plasma treatment, the contact angle increased in the hexagonal partition wall structure, whereas it decreased in the triangular partition wall structure.

4.2 Durability Test

To evaluate the abrasion resistance of the imprint film surface, a pin-on-disc experiment was performed using an abrasion tester (YASUDA Co, No.101 HS), and ASTM G99 was used for the test specifications. The abrasion material was silicone rubber, and a truncated cone shape with a contact surface diameter of 4 mm was used. The load was measured using Tekscan's flexible A301 sensor with a test load of 70 g. The test was performed 1000–10,000 times at a speed of 60 rpm in a dry wear environment.

In order to verify the performance of the proposed structure, the contact pressure applied to the pillar structure should be applied uniformly, but there are practical limitations. Also, from a scientific point of view, it is exact to compare the pure pillar structure and optimum hexagonal structure. However, since the pure pillar structure has too low mechanical durability, it is not easy to experiment in reality. Therefore, in this study, durability was evaluated depending on whether the hexagonal partition wall structure was optimized, and the performance of the optimal structure was verified.

The abrasion resistance of the hexagonal partition wall structure before and after applying the optimal design was compared, as shown in Figs. 3 and 5. In the imprint film without CF4 plasma treatment, the wear resistance was evaluated by changing the contact angle before and after the pin-on-disc experiment. The contact angle was measured by moving the wear marks. Table 5 shows the measurement results of the contact angles before and after the wear test. The change in contact angle by the pins used in the disc test was less than $\pm 5°$ after performing the test for 1000 to 5000 times, and it was discovered that measurement errors such as

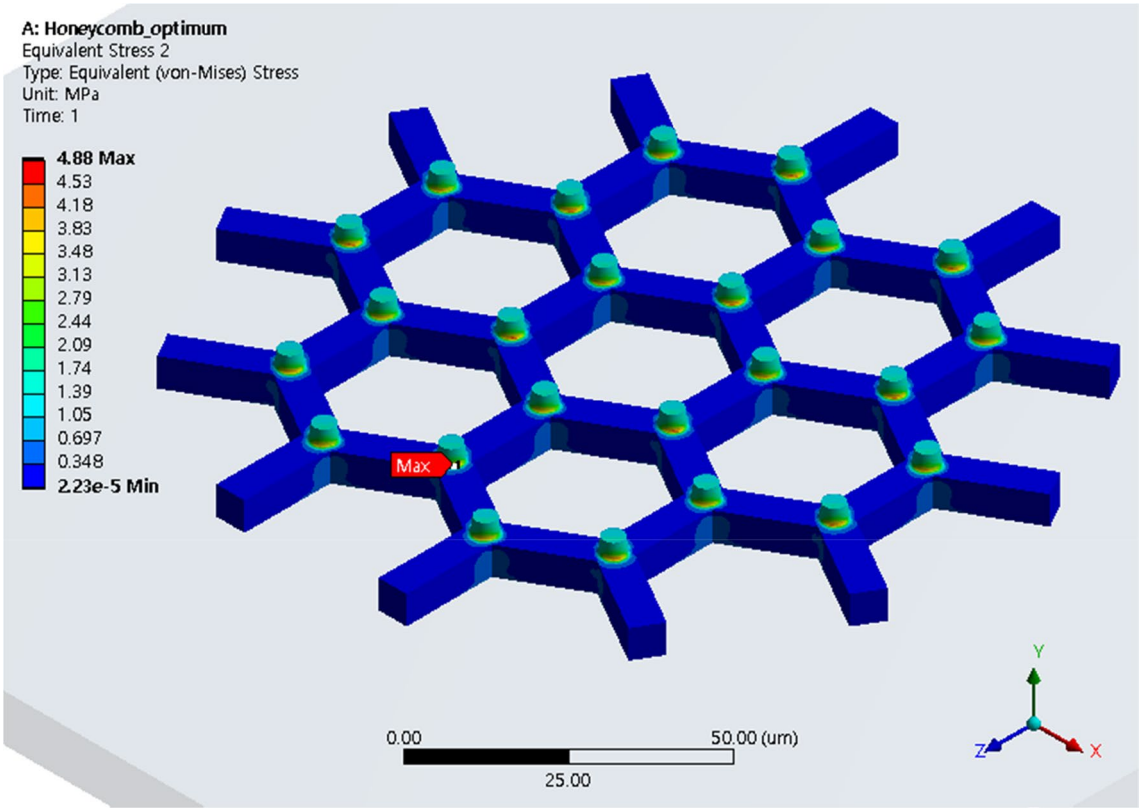

Fig. 5 Distribution of maximum stress generated when honeycomb structure was subjected to load

Table 4 Comparison results of maximum stress distribution caused by change in bulkhead morphology

Surface morphology	Bulkhead morphology		
	Honeycomb	Triangle	Square
Micropillar array	16.83		
Hierarchical reference	7.93	8.27	8.10
Hierarchical optimum	4.88	4.51	4.34

measurement position changes and baseline position errors in solid and liquid interfaces occurred.

The optimal shape after 10,000 wear tests indicated a change in contact angle of less than ± 5°; however, in the reference shape before the optimal design was applied, the contact angle decreased by 11.6° on average. Figure 10 shows the optical microscope image of the imprint film that underwent 2000 pin-on-disc experiments. Wear marks were identified on the surface on which wear tests were performed up to 2000 times, and the shape of the pillar structure was identified. The SEM image of the surface subjected to 10,000 abrasion tests is shown in Fig. 11. The low height of the pillar before the wear test was identified as a defect caused by insufficient PUA resin filling the space of the PDMS mold during the imprinting process. Although the silicon rubber adhered onto the surface via heat generated in a dry environment without lubrication, the partition wall structure and pillar structure of the surface were verifiable even after 10,000 pin-on-disc tests.

5 Conclusion

A surface shape to increase the durability of a superhydrophobic surface structure was presented hereinabove. An optimal design was determined based on the design of experiments and finite element analysis. Prototypes were processed via micro 3D printing, and ultra-water-repellent films were fabricated via UV-imprint lithography.

The stress distribution generated in the pillar structure under load conditions was analyzed, and a structure for distributing the stress concentration was proposed. The proposed structure was a hierarchical structure, in which the space between pillars was connected by a partition wall structure. Meanwhile, the upper/lower diameter and height of the pillar, the height and thickness of the partition wall, and the interval between the pillars were selected as design variables. Compared with the pillar structure under the same load conditions, the maximum stress generated in the optimal shape decreased by approximately 71%.

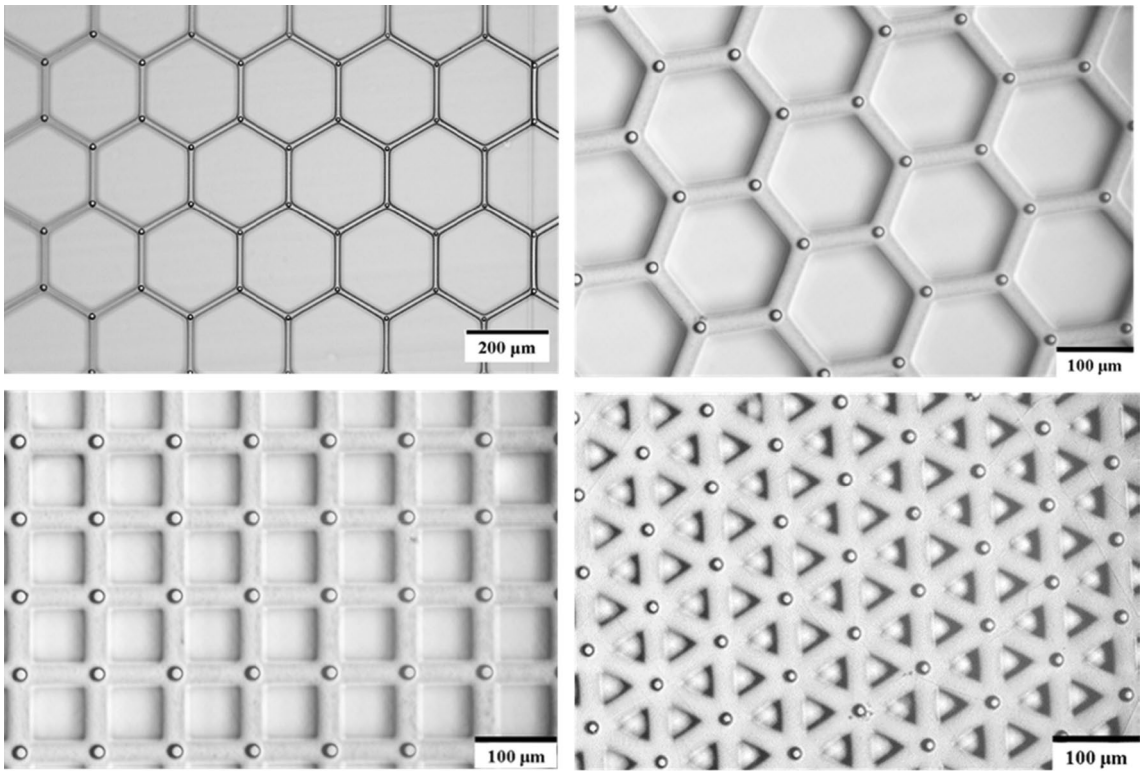

Fig. 6 Optical microscope image of prototype surface fabricated via PµSL. Clockwise from top left: reference, honeycomb, triangle, and square optimum structures

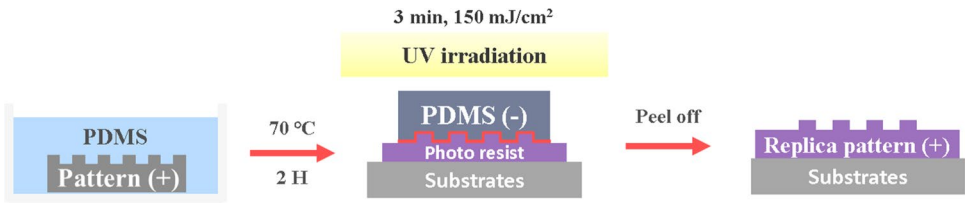

Fig. 7 Replica pattern processed on PET film via UV-imprint lithography

Prototypes of the reference shape and optimal shape of the hierarchical structure were processed via micro 3D printing. The processed shape was replicated on a PET film using a PDMS mold via UV-imprint lithography. The shape of the partition wall was evaluated by processing hexagonal, triangular, and square structures. The contact angle for the hexagonal partition wall structure was the highest, as analyzed using the Cassie–Baxter model; the lower the contact fraction of the solid surface, the higher was the contact angle.

The pin-on-disc test was conducted 1000–10,000 times using silicone rubber to verify the durability of the processed super-water repellent surface. In terms of the optimal shape, the change in contact angle was only ± 5° even after 10,000 pin-on-disc tests; however, the contact angle of the reference shape decreased by approximately 11.6°.

In future, we plan to compare the wetting characteristics of various pillar shapes via micro 3D printing.

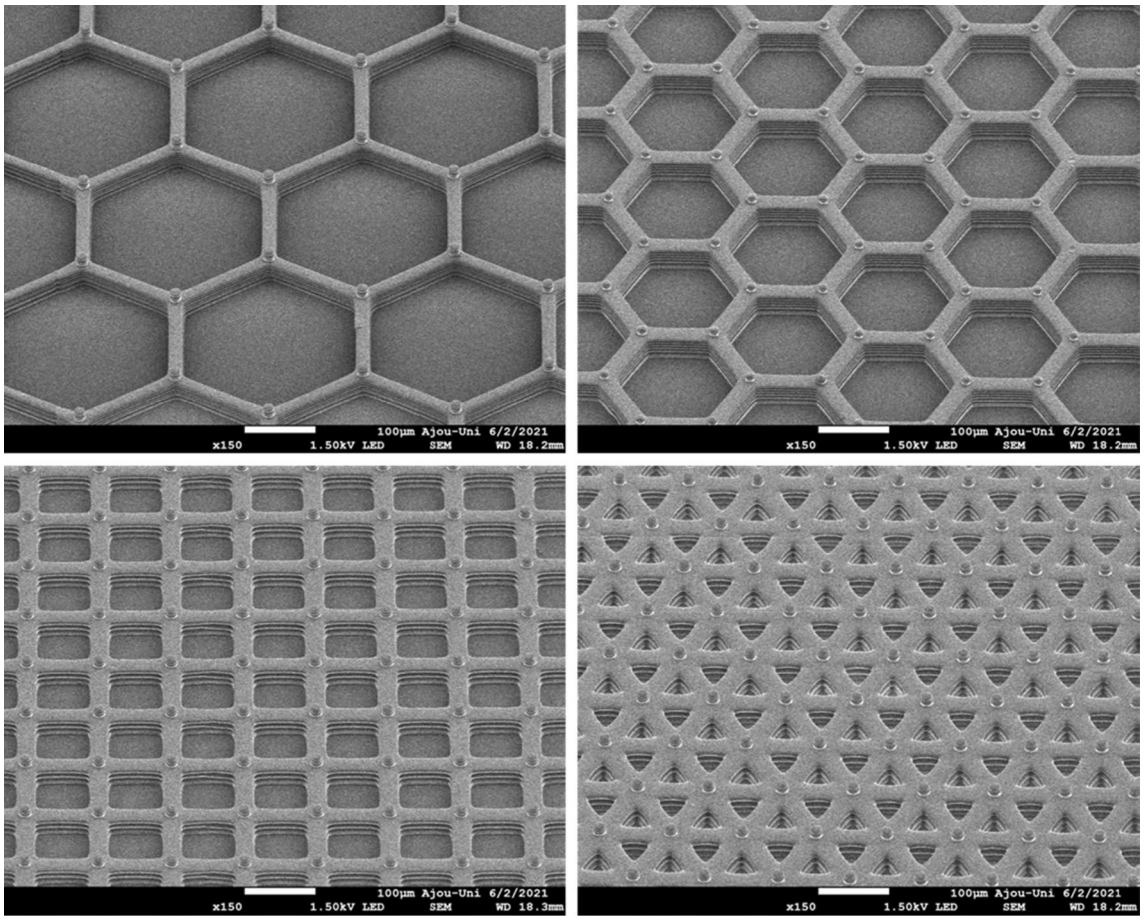

Fig. 8 SEM image of replica pattern obtained via UV-imprint lithography. Clockwise from top left: reference, honeycomb, triangle, and square optimum structures

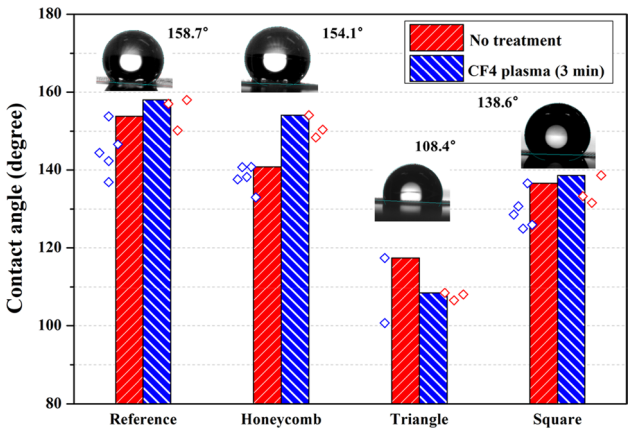

Fig. 9 Amount of change in contact angle before and after CF_4 plasma treatment

Table 5 Results of contact angle measurements before and after pin-on-disc experiment; average value and amount of change in contact angle before and after the wear test

Test condition			Contact angle (°)					Average	ΔCA
			Number of measurements						
Cycle	Type	Wear (Y/N)	1	2	3	4	5		
1000	R	N	151	146.8	147.1	149.5	149.7	148.8	−0.3
		Y	146.3	146.4	147.4	148.2	154.4	148.5	
	O	N	135.4	135.8	138.8	141.1	149.5	140.1	2.5
		Y	139.1	139.7	140.6	144.6	148.9	142.6	
2000	R	N	144.5	147.1	148.5	148.9	149.4	147.7	−3.3
		Y	128	140.9	148.4	151.3	153.6	144.4	
	O	N	138.5	138.7	139.5	141.3	141.5	139.9	−3.6
		Y	132.2	135.4	136.7	137.3	139.7	136.3	
5000	R	N	142.5	143.9	145.5	146.5	153	146.3	−2.3
		Y	136	143.7	147.7	149.2	143.2	144.0	
	O	N	133.6	137.8	138.8	139.7	139.7	137.9	0.6
		Y	141.9	134.3	137.7	139.1	139.6	138.5	
10,000	R	N	144.9	145.1	145.3	145.7	147.3	145.7	−11.6
		Y	127.5	132.2	135.4	136.9	138.4	134.1	
	O	N	130.2	131.1	133	133.2	134.4	132.4	1.6
		Y	131.9	132.9	134.6	135.2	135.4	134	

**R* reference structures, *O* optimal design structures based on design of experiments, *N* imprinted film before wear test, and *Y* imprinted film after wear test

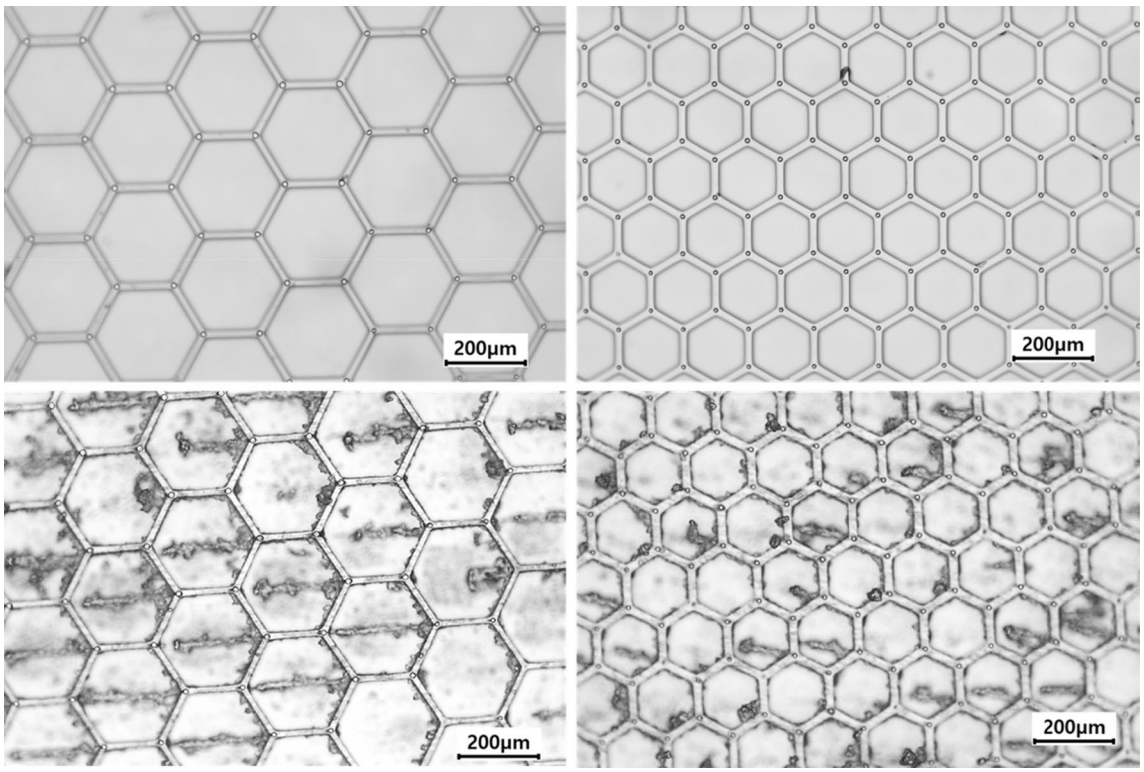

Fig. 10 Optical microscope image of imprinted film after 2000 cycles of pin-on-disc test. Upper image shows reference (left) and optimum (right) structures before pin-on-disc test; lower images show the corresponding surfaces after the abrasion test

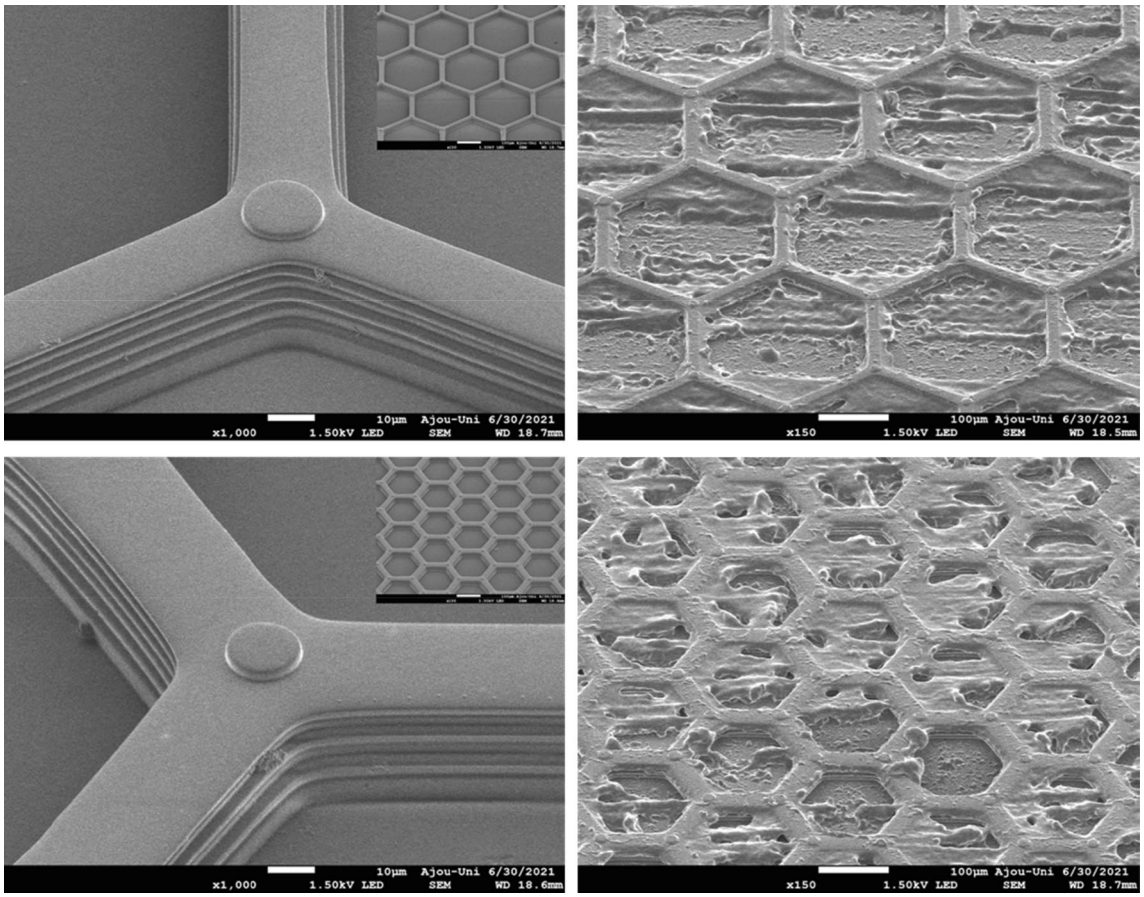

Fig. 11 SEM image of imprinted film after 10,000 cycles of pin-on-disc test. Upper images show surface of reference structures; lower images correspond to optimum structure. Left side shows surface before wear in each structure, and right side shows surface after wear

Acknowledgements This study was supported by the Ministry of Trade, Industry, and Energy (MOTIE, Korea) under the Industrial Technology Innovation Program (No. 20000665). The authors would like to thank Editage (www.editage.co.kr) for English language editing.

References

1. Zhang, X., Guo, Y., Zhang, Z., & Zhang, P. (2013). Self-cleaning superhydrophobic surface based on titanium dioxide nanowires combined with polydimethylsiloxane. *Applied Surface Science, 284*, 319–323. https://doi.org/10.1016/j.apsusc.2013.07.100
2. Qu, Z., Wang, F., Liu, P., Yu, Q., & Brouwers, H. (2020). Super-hydrophobic magnesium oxychloride cement (MOC): From structural control to self-cleaning property evaluation. *Materials and Structures, 53*(2), 1–10. https://doi.org/10.1617/s11527-020-01462-3
3. Xu, M., Grabowski, A., Yu, N., Kerezyte, G., Lee, J.-W., & Pfeifer, B. R. (2020). Superhydrophobic drag reduction for turbulent flows in open water. *Physical Review Applied, 13*(3), 034056. https://doi.org/10.1103/PhysRevApplied.13.034056
4. Dong, H., Cheng, M., Zhang, Y., Wei, H., & Shi, F. (2013). Extraordinary drag-reducing effect of a superhydrophobic coating on a macroscopic model ship at high speed. *Journal of Materials Chemistry A, 1*(19), 5886–5891. https://doi.org/10.1039/C3TA10225D
5. Cao, L., Jones, A. K., Sikka, V. K., Wu, J., & Gao, D. (2009). Anti-icing superhydrophobic coatings. *Langmuir, 25*(21), 12444–12448. https://doi.org/10.1021/la902882b
6. Barthwal, S., & Lim, S.-H. (2020). Robust and chemically stable superhydrophobic aluminum-alloy surface with enhanced corrosion-resistance properties. *International Journal of Precision Engineering and Manufacturing-Green Technology, 7*(2), 481–492. https://doi.org/10.1007/s40684-019-00031-6
7. Leslie, D. C., Waterhouse, A., Berthet, J. B., Valentin, T. M., Watters, A. L., Jain, A., Kim, P., Hatton, B. D., Nedder, A., Donovan, K., Super, E. H., Howell, C., Johnson, C. P., Vu, T. L., Bolgen, D. E., Rifai, S., Hansen, A. R., Aizenberg, M., Super, M., … Ingber, D. E. (2014). A bioinspired omniphobic surface coating on medical devices prevents thrombosis and biofouling. *Nature biotechnology, 32*(11), 1134–1140. https://doi.org/10.1038/nbt.3020
8. Bartlet, K., Movafaghi, S., Dasi, L. P., Kota, A. K., & Popat, K. C. (2018). Antibacterial activity on superhydrophobic titania nanotube arrays. *Colloids and Surfaces B: Biointerfaces, 166*, 179–186. https://doi.org/10.1016/j.colsurfb.2018.03.019
9. Zhang, P., & Lv, F. (2015). A review of the recent advances in superhydrophobic surfaces and the emerging energy-related applications. *Energy, 82*, 1068–1087. https://doi.org/10.1016/j.energy.2015.01.061

10. Vazirinasab, E., Jafari, R., & Momen, G. (2018). Application of superhydrophobic coatings as a corrosion barrier: A review. *Surface and Coatings Technology, 341*, 40–56. https://doi.org/10.1016/j.surfcoat.2017.11.053
11. Jeevahan, J., Chandrasekaran, M., Joseph, G. B., Durairaj, R., & Mageshwaran, G. (2018). Superhydrophobic surfaces: A review on fundamentals, applications, and challenges. *Journal of Coatings Technology and Research, 15*(2), 231–250. https://doi.org/10.1007/s11998-017-0011-x
12. Ellinas, K., Tserepi, A., & Gogolides, E. (2017). Durable superhydrophobic and superamphiphobic polymeric surfaces and their applications: A review. *Advances in Colloid and Interface Science, 250*, 132–157. https://doi.org/10.1016/j.cis.2017.09.003
13. Dalawai, S. P., Aly, M. A. S., Latthe, S. S., Xing, R., Sutar, R. S., Nagappan, S., Ha, C., Sadasivuni, K. K., & Liu, S. (2020). Recent advances in durability of superhydrophobic self-cleaning technology: A critical review. *Progress in Organic Coatings, 138*, 105381. https://doi.org/10.1016/j.porgcoat.2019.105381
14. Barthlott, W., & Neinhuis, C. (1997). Purity of the sacred lotus, or escape from contamination in biological surfaces. *Planta, Original Paper, 202*(1), 1–8. https://doi.org/10.1007/s004250050096
15. Cheng, Q., Li, M., Zheng, Y., Su, B., Wang, S., & Jiang, L. (2011). Janus interface materials: Superhydrophobic air/solid interface and superoleophobic water/solid interface inspired by a lotus leaf. *Soft Matter, 7*(13), 5948–5951. https://doi.org/10.1039/C1SM05452J
16. Bhushan, B., Jung, Y. C., & Koch, K. (2009). Micro-, nano-and hierarchical structures for superhydrophobicity, self-cleaning and low adhesion. *Philosophical Transactions of the Royal Society A: Mathematical, Physical and Engineering Sciences, 367*(1894), 1631–1672. https://doi.org/10.1098/rsta.2009.0014
17. Zhang, D., Williams, B. L., Shresth, S. B., Nasir, Z., Becher, E. M., Lofink, B. J., Santos, V. H., Patel, H., Peng, X., & Sun, L. (2017). Flame retardant and hydrophobic coatings on cotton fabrics via sol-gel and self-assembly techniques. *Journal of Colloid and Interface Science, 505*, 892–899. https://doi.org/10.1016/j.jcis.2017.06.087
18. Ishizaki, T., Hieda, J., Saito, N., & Takai, O. (2010). Corrosion resistance and chemical stability of super-hydrophobic film deposited on magnesium alloy AZ31 by microwave plasma-enhanced chemical vapor deposition. *Electrochimica Acta, 55*(23), 7094–7101. https://doi.org/10.1016/j.electacta.2010.06.064
19. Liu, Q., Chen, D., & Kang, Z. (2015). One-step electrodeposition process to fabricate corrosion-resistant superhydrophobic surface on magnesium alloy. *ACS Applied Materials & Interfaces, 7*(3), 1859–1867. https://doi.org/10.1021/am507586u
20. Zhang, B., Li, Y., & Hou, B. (2015). One-step electrodeposition fabrication of a superhydrophobic surface on an aluminum substrate with enhanced self-cleaning and anticorrosion properties. *RCS Advances, 5*(121), 100000–100010. https://doi.org/10.1039/C5RA21525K
21. Ryu, J., Kim, K., Park, J., Hwang, B., Ko, Y., Kim, H., Han, J., Seo, E., Park, Y., & Lee, S. (2017). Nearly perfect durable superhydrophobic surfaces fabricated by a simple one-step plasma treatment. *Scientific Reports, 7*(1), 1–8. https://doi.org/10.1038/s41598-017-02108-1
22. Alameda, M. T., Osorio, M. R., Hernández, J. J., & Rodríguez, I. (2019). Multilevel hierarchical topographies by combined photolithography and nanoimprinting processes to create surfaces with controlled wetting. *ACS Applied Nano Materials, 2*(8), 4727–2733. https://doi.org/10.1021/acsanm.9b00338
23. Yang, Z., Liu, X., & Tian, Y. (2020). Novel metal-organic superhydrophobic surface fabricated by nanosecond laser irradiation in solution. *Colloids and Surfaces A: Physicochemical and Engineering Aspects, 587*, 124343. https://doi.org/10.1016/j.colsurfa.2019.124343
24. Martínez-Calderon, M., Rodríguez, A., Dias-Ponte, A., Morant-Miñana, M., Gómez-Aranzadi, M., & Olaizola, S. (2016). Femtosecond laser fabrication of highly hydrophobic stainless steel surface with hierarchical structures fabricated by combining ordered microstructures and LIPSS. *Applied Surface Science, 374*, 81–89. https://doi.org/10.1016/j.apsusc.2015.09.261
25. Susarrey-Arce, A., Marín, Á. G., Schlautmann, S., Lefferts, L., Gardeniers, J. G., & van Houselt, A. (2012). One-step sculpting of silicon microstructures from pillars to needles for water and oil repelling surfaces. *Journal of Micromechanics and Microengineering, 23*(2), 025004. https://doi.org/10.1088/0960-1317/23/2/025004
26. Sun, T., Wang, G., Liu, H., Feng, L., Jiang, L., & Zhu, D. (2003). Control over the wettability of an aligned carbon nanotube film. *Journal of the American Chemical Society, 125*(49), 14996–14997. https://doi.org/10.1021/ja038026o
27. Wang, T., Zhu, H., Zhang, Z., Gao, J., Wu, Y., Hu, M., & Xu, K. (2021). Preparing of superamphiphobic surface by fabricating hierarchical nano re-entrant pyramids on micro-cones using a combined laser-electrochemistry method. *Surfaces and Interfaces, 24*, 101112. https://doi.org/10.1016/j.surfin.2021.101112
28. Kehagias, N., Francone, A., Guttmann, M., Winkler, F., Fernández, A., & Sotomayor Torres, C. M. (2018). Fabrication and replication of re-entrant structures by nanoimprint lithography methods. *Journal of Vacuum Science & Technology B, Nanotechnology and Microelectronics: Materials, Processing, Measurement, and Phenomena, 36*(6), 06JF01. https://doi.org/10.1116/1.5048241
29. Kodihalli Shivaprakash, N., Zhang, J., Panwar, A., Barry, C., Truong, Q., & Mead, J. (2019). Continuous manufacturing of reentrant structures via roll-to-roll process. *Journal of Applied Polymer Science, 136*(1), 46980. https://doi.org/10.1002/app.46980
30. Lin, Y., Zhou, R., & Xu, J. (2018). Superhydrophobic surfaces based on fractal and hierarchical microstructures using two-photon polymerization: Toward flexible superhydrophobic films. *Advanced Materials Interfaces, 5*(21), 1801126. https://doi.org/10.1002/admi.201801126
31. Dong, Z., Schumann, M. F., Hokkanen, M. J., Chang, B., Welle, A., Zhou, Q., Ras, R. H. A., Xu, Z., Wegener, M., & Levkin, P. A. (2018). Superoleophobic slippery Lubricant-Infused surfaces: Combining two extremes in the same surface. *Advanced Materials, 30*(45), 1803890. https://doi.org/10.1002/adma.201803890
32. Darband, G. B., Aliofkhazraei, M., Khorsand, S., Sokhanvar, S., & Kaboli, A. (2020). Science and engineering of superhydrophobic surfaces: Review of corrosion resistance, chemical and mechanical stability. *Arabian Journal of Chemistry, 13*(1), 1763–1802. https://doi.org/10.1016/j.arabjc.2018.01.013
33. Golovin, K., Boban, M., Mabry, J. M., & Tuteja, A. (2017). Designing self-healing superhydrophobic surfaces with exceptional mechanical durability. *ACS Applied Materials & Interfaces, 9*(12), 11212–11223. https://doi.org/10.1021/acsami.6b15491
34. Chen, X., Gong, Y., Li, D., & Li, H. (2016). Robust and easy-repairable superhydrophobic surfaces with multiple length-scale topography constructed by thermal spray route. *Colloids and Surfaces A: Physicochemical and Engineering Aspects, 492*, 19–25. https://doi.org/10.1016/j.colsurfa.2015.12.017
35. Xiu, Y., Liu, Y., Hess, D. W., & Wong, C. (2010). Mechanically robust superhydrophobicity on hierarchically structured Si surfaces. *Nanotechnology, 21*(15), 155705. https://doi.org/10.1088/0957-4484/21/15/155705
36. Wenzel, R. N. (1936). Resistance of solid surfaces to wetting by water. *Industrial & Engineering Chemistry, 28*(8), 988–994. https://doi.org/10.1021/ie50320a024

37. Cassie, A., & Baxter, S. (1944). Wettability of porous surfaces. *Transactions of the Faraday society, 40*, 546–551. https://doi.org/10.1039/TF9444000546
38. Peters, R. M., Hackeman, E., & Goldreich, D. (2009). Diminutive digits discern delicate details: Fingertip size and the sex difference in tactile spatial acuity. *Journal of Neuroscience, 29*(50), 15756–15761. https://doi.org/10.1523/JNEUROSCI.3684-09.2009

Yousung Kang received the B.S., M.S., and Ph.D. degrees in mechanical engineering from Ajou University, South Korea, in 2015, 2017, and 2021, respectively. He is currently a Post-Doctorate researcher at the Electronics and Telecommunications Research Institute (ETRI), South Korea. His research interests are printed electronics and Electrodes for Deep brain stimulation in neuroscience.

Gayun Jang is a B.S. candidate in the Department of Mechanical Engineering from Ajou University, South Korea. Her research interests are manufacturing processes.

Ga Eul Kim is currently a researcher at the Korea Institute Machinery & Materials (KIMM), South Korea. He received his B.S. degree in mechanical engineering from Ajou University, South Korea, in 2014. He received his M.S. and Ph.D. degrees from Ajou University, South Korea, in 2017 and 2022, respectively. His research interests include roll-to-roll processing systems and pressure uniformity control for the roll-to-roll system.

Sin Kwon a principal researcher at the Korea Institute of Machinery & Materials (KIMM), Daejeon, Korea. He received his BS in 1997, MS in 1999 and PhD in 2005 from the Department of Mechanical Engineering at KAIST (Korea Advanced Institute of Science & Technology). He joined Manufacturing Technology Center at Samsung Electronics as a senior research engineer from 2005 to 2013. His research interests focus mainly on the R&D of roll-to-roll processing/printing system for printed electronics.

Moon G. Lee received the B.S. degree in precision engineering and the M.S. and Ph.D. degrees in mechanical engineering from the Korea Advanced Institute of Science and Technology (KAIST), Daejeon, Korea, in 1995, 1997, and 2003, respectively. He became a Senior Researcher for Samsung Electronics in Suwon, Korea. He is currently a professor in the Dept. of Mechanical Engineering, Ajou University, Suwon, Korea. His research interests include design and control of high precision positioning systems, nanoimprinting systems, and biomedical devices.

Yongho Jeon is currently a Professor in the Department of Mechanical Engineering at Ajou University. He received his B.S. degree in mechanical engineering from Ajou University, South Korea and the Illinois Institute of Technology, USA, in 2003. He received his M.S. and Ph.D. degrees from the University of Wisconsin, Madison, Wisconsin, USA, in 2005 and 2008, respectively. His research interests are developing novel manufacturing processes using heat and vibration and their effects of processes on the material characteristics.